

Supplementary Information for:

Oxygen Exchange Kinetics on Systematically Doped Ceria: A Pulsed Isotope Exchange Study

M. Schaube, R. Merkle, J. Maier

Max-Planck-Institute for Solid State Research, Stuttgart, Germany

1 Quantification and of Oxygen Isotopologues and Error Discussion

The peak areas A for each molecular oxygen isotope species i at a reactor temperature T were normalized by the peak area of the $^{15}\text{N}_2$ signal (A_{30}),

$$N_i(T) = \left| \frac{A_i(T_R) - A_i(T)}{A_{30}(T)} \right| \quad (1)$$

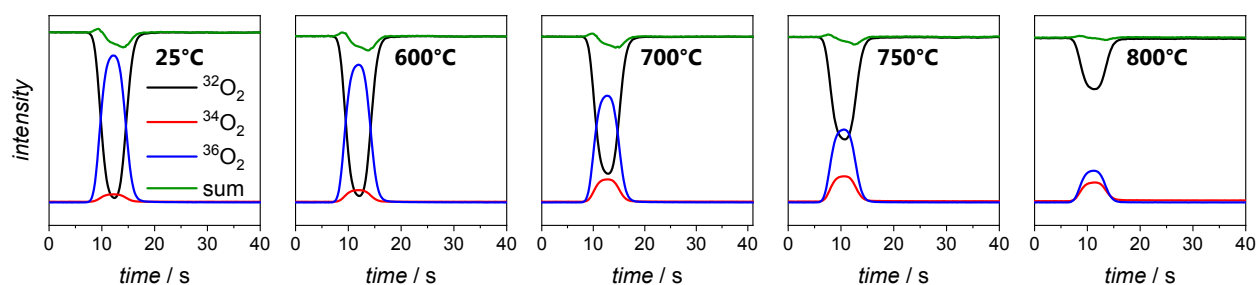
where T_R is the reference temperature where no oxygen exchange occurs (usually $T_R = 25^\circ\text{C}$). The molecular oxygen isotope fractions f were calculated by

$${}^{32}f = \frac{N_{32}(T)}{\sum_i N_i(T)} + {}^{32}f_0 \quad {}^{34}f = \frac{N_{34}(T)}{\sum_i N_i(T)} + {}^{34}f_0 \quad {}^{36}f = \frac{N_{36}(T)}{\sum_i N_i(T)} + {}^{36}f_0 - 1 \quad (2)$$

in which f_0 represents the initial molar fractions in the 97 at% enriched ^{18}O gas prior to isotope exchange. The values for ${}^{32}f_0$, ${}^{34}f_0$, and ${}^{36}f_0$ can be calculated by assuming statistical equilibrium of oxygen isotopes in the isotope enriched gas (square brackets denote concentrations)

$${}^{18}\text{O}^{18}\text{O} + {}^{16}\text{O}^{16}\text{O} \rightleftharpoons 2{}^{18}\text{O}^{16}\text{O} \quad \frac{[{}^{18}\text{O}^{16}\text{O}]^2}{[{}^{18}\text{O}_2][{}^{16}\text{O}_2]} = 4 \quad (3)$$

and are 0.001, 0.056 and 0.943. The total isotope fraction ${}^{18}f$ is obtained according to ${}^{18}f = {}^{36}f + 0.5{}^{34}f$.



ESI Figure 1: PIE raw data for 20GDC. Depicted are the ion currents for the three oxygen isotopomers as a function of time. The green line displays the sum of the oxygen signals and represents the mass balance.

In ESI Figure 1 the monitored pulse response at the exit of the reactor for signals at $m/z = 32$ ($^{16}\text{O}_2$), 34 ($^{18}\text{O}^{16}\text{O}$), and 36 ($^{18}\text{O}_2$) with resolution of five points per second for 20GDC is displayed. During pulsing the sum of the oxygen signals (green line) deviates slightly from the ${}^{32}\text{O}_2$ signal, but this small deviation from mass balance does not perceptibly alter the values for calculated fractions or reaction rates. The

sum of the peak areas remains almost constant in a T -series and shows only deviations of $\pm 0.5\%$ (low T , low oxygen conversion) to $\pm 5\%$ (high T and high oxygen conversion).

Typically, the relative measurement uncertainties for ^{32}f , ^{34}f , and ^{36}f during PIE range between $\pm 2\%$ and $\pm 6\%$ and are higher for ^{32}f and ^{34}f at high temperatures and with samples which show a moderate formation of $^{34}\text{O}_2$ (overlap of incorporation/excorporation). It is worth noting that the error becomes larger for high isotope conversion. The variation of \mathfrak{R}_0 (defined in eq. 8, main text) with T or $p(\text{O}_2)$ was measured without removing the sample from the reactor; correspondingly the uncertainty on E_a and exponent of $p(\text{O}_2)$ dependence is small. Repetition of the T -series (without removing the sample from reactor and reactor from furnace) did not show any indications of sample degradation. However, when three fresh 20PDC samples were mounted, the \mathfrak{R}_0 values varied by a factor of 0.3 – 1.7 relative to the mean value at low oxygen conversion, but with increasing T and conversion this deviation decreased. This is partly related to variations in the pressure drop across the catalyst bed which modifies the residence time, as well as minor T variations (the thermocouple is situated close the catalyst bed but not inside). The relative error for extracted E_a values amounts $\pm 5\%$. Since in the plot of dopant dependence (Figure 7, main text) the dopant concentrations are varied over a large range by 1.5 orders of magnitude, the slopes in this figure are nevertheless reliable.

2 Bulk vs. Surface Defect Regimes

ESI Table 1: Surface *vs.* bulk defect regimes. Different situations regarding the $p(O_2)$ dependence of defects at the surface are displayed and compared to the expected dependencies in the bulk material of intrinsic, acceptor, and donor doped ceria. Σ denotes the surface charge density, n_i the exponent of the $p(O_2)$ dependence of defect i .

	Surface Regime	Bulk Regimes				Surface Regime
		Intrinsic	Acceptor	Donor		
		$2[V_{O}^{\bullet\bullet}]_b = [e']_b$ $n_{V,b} = n_{e,b} = 1/6$	$2[V_{O}^{\bullet\bullet}]_b = [Gd']_b$ $\Rightarrow [V_{O}^{\bullet\bullet}]_b = const.$ $n_{e,b} = -1/4$	$[Nb^{\bullet}]_b = [e']_b$ $\Rightarrow [e']_b = const.$ $n_{O_i,b} = 1/2$	$2[O_i'']_b = [Nb^{\bullet}]_b$ $\Rightarrow [O_i'']_b = const.$ $n_{e,b} = -1/4$	
1	$\Sigma = 0$ $2[V_{O}^{\bullet\bullet}]_s = [e']_s$ $n_{V,s} = n_{e,s} = 1/6$	equal n	different n	equal n	different n	$\Sigma = 0$ $[Nb^{\bullet}]_s = [e']_s$ $n_{O_i,s} = 1/2$
2	$\Sigma = 0$ $2[V_{O}^{\bullet\bullet}]_s = [Gd']_s$ $n_{e,s} = -1/4$	different n	equal n	different n	equal n	$\Sigma = 0$ $[O_i'']_s = [Nb^{\bullet}]_s$ $n_{e,s} = -1/4$
3	$\Sigma \neq 0$ $\Sigma \approx 2[V_{O}^{\bullet\bullet}]_s = const.$ $n_{e,s} = -1/4$	different n	equal n	different n	equal n	$\Sigma \neq 0$ $\Sigma \approx 2[O_i'']_s = const.$ $n_{e,s} = -1/4$
4	$\Sigma \neq 0$ $\Sigma \approx [e']_s = const.$ $n_{V,s} = -1/2$	different n	different n	equal n	different n	$\Sigma \neq 0$ $\Sigma \approx [e']_s = const.$ $n_{O_i,s} = -1/2$
5	$\Sigma \neq 0$ but small $K = K_{\infty} \exp(-\frac{zF\theta}{RT})$ $n_{e,s} = -x$ $n_{V,s} = -2n_{e,s} - 1/2$	different n	different n	different n	different n	$\Sigma \neq 0$ but small $K = K_{\infty} \exp(-\frac{zF\theta}{RT})$ $n_{e,s} = -x$ $n_{V,s} = -2n_{e,s} - 1/2$

<div style="display: flex; flex-direction: column; gap: 5px;"> <div style="background-color: #d9ead3; width: 20px; height: 10px; display: inline-block;"></div> Realistic Cases</div> <div style="background-color: #f4cccc; width: 20px; height: 10px; display: inline-block;"></div> Less Realistic Cases

In ESI Table 1, different situations regarding the oxygen partial pressure dependence at the surface and in the bulk are compared. In general, the absolute surface defect concentrations will differ from the bulk values, but the $p(O_2)$ dependences may differ or not. Furthermore, the surface layer may carry an excess charge density Σ . In the following some cases are discussed in detail, *cf.* also the discussion in the Appendix C of¹. Cases which are in principle realistic are marked with green, less realistic cases are in red and cases which are hard to estimate are in purple. We will start the discussion by first giving an overview of the possible defect chemical regimes that can occur at the surface (cases 1 to 5) followed by a specific discussion of intrinsic and doped ceria.

In the first two cases a zero surface charge density arises if:

- (1) Surface oxygen vacancies ($V_{O,s}^{\bullet\bullet}$) are compensated by surface electrons (e'_s), then the $p(O_2)$ dependency of $[V_{O,s}^{\bullet\bullet}]$ and $[e'_s]$ is 1/6.
- (2) $V_{O,s}^{\bullet\bullet}$ are compensated and pinned by surface acceptor dopants ($A_{Ce,s}^{\bullet}$), this yields a proportionality of $[e'_s]$ to $p(O_2)^{1/4}$

If ceria has a non-zero surface charge, the sign of this surface charge is expected to be positive. Positive excess charges have been found for grain boundary cores in ceria (see, e.g.,²) and zirconia electrolyte materials, and for a YSZ bicrystal a $V_{O}^{\bullet\bullet}$ accumulation in the grain boundary core has been evidenced by TEM³. Surface

defect concentrations of ceria films have been measured by ambient-pressure XPS⁴⁻⁷ leading to the conclusion that the surface charges are small. However, in ref.^{2, 8} it is discussed that the data in ref.⁷ might also be interpreted by a surface space charge potential (corresponding to a positive excess charge) that is independent of applied dc bias, *i.e.* independent of the oxygen chemical potential in the film. Kinetic Monte Carlo simulations yielded a small positive excess surface charge (approx. +2 elementary charges per surface unit cell which comprises 128 ceria formula units) for 10 mol% Gd-doped ceria⁹.

Three further cases can be distinguished when Σ shows a non-zero value:

- (3) Σ is large and determined by $V_{o,s}^{\bullet\bullet}$, meaning that $[V_{o,s}^{\bullet\bullet}]$ is relatively high. Therefore, $[V_{o,s}^{\bullet\bullet}]$ is to a good approximation $p(O_2)$ independent, and $[e_s']$ is proportional to $p(O_2)^{-1/4}$.
- (4) Here, Σ is determined by $[e_s']$ and the $p(O_2)$ dependence of $[V_{o,s}^{\bullet\bullet}]$ is $-1/2$. However, this case does not apply for ceria, see above.
- (5) The last case corresponds to a small Σ , which implies that Σ itself may have a perceptible $p(O_2)$ dependence. This makes it hard to derive analytical expressions for the $p(O_2)$ dependency of surface defects.

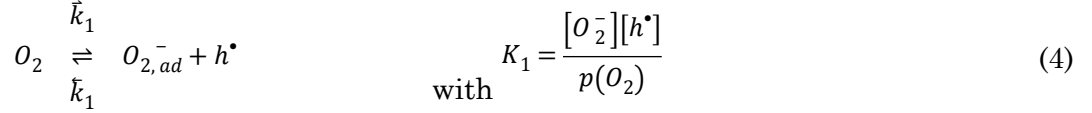
Whenever the same majority carrier prevails for bulk and surface, bulk and surface defects exhibit the same $p(O_2)$ dependencies. In case of undoped ceria⁴ in reducing conditions the excess concentrations of $V_{o,s}^{\bullet\bullet}$ and e_s' were found to match almost perfectly so that Σ is rather small; thus we assume case (1) also for the present undoped ceria samples. For Sm-doped ceria the quantification of surface $V_{o,s}^{\bullet\bullet}$ and $Ce_{ce,s}'$ indicated that under reducing conditions they largely mutually charge-compensate⁶. Pr-doped ceria films in intermediate to high $p(O_2)$ were argued to have no pronounced surface charge^{5, 10}. For acceptor-doped ceria, also a constant surface charge density (case (3)) leads to the same defect regime with constant $[V_{o,s}^{\bullet\bullet}]$ as case (2) with negligible surface charge. Approximately $p(O_2)$ independent space charge potentials and corresponding approximately constant excess charges have been observed for grain boundaries in ref.¹¹ for Fe-doped SrTiO₃. Overall, for undoped as well as acceptor doped ceria we can reasonably assume the same $p(O_2)$ dependencies of surface and bulk defects.

For donor-doped ceria, no direct measurements of surface defect concentrations are available so far, but again a number of probable cases yield the same defect chemical regimes for surface and bulk.

3 Influences of electron holes to the equilibrium exchange rate

Reaction (10) in the main paper is not an elementary reaction, but involves the formation of charged molecular adsorbates as fast preceding equilibrium, *e.g.* as given by reaction (4) below. As a consequence, the rate constant \bar{k}_{da} in the main paper may itself depend on defect concentrations, leading to a modified overall dependence.

The modified proportionality $\mathfrak{R}_0 \propto p(O_2)^{3/4} \propto [V_o^{\bullet\bullet}]^{1/2}$ can be obtained by assuming that the fast pre-equilibrium involves one electron hole:



The overall equilibrium exchange rate \mathfrak{R}_0 (6) equals the reaction rate of dissociative incorporation as displayed in (5) which represents the rate-determining step for oxygen incorporation.



$$\mathfrak{R}_0 = \bar{k}_2 [O_2^-][V_o^{\bullet\bullet}] = \bar{k}_2 K_1 p(O_2) [V_o^{\bullet\bullet}] [h^\bullet]^{-1} \quad (6)$$

Substitution of $[h^\bullet]$ in (6) with *eq.* (2) of the main text finally yields:

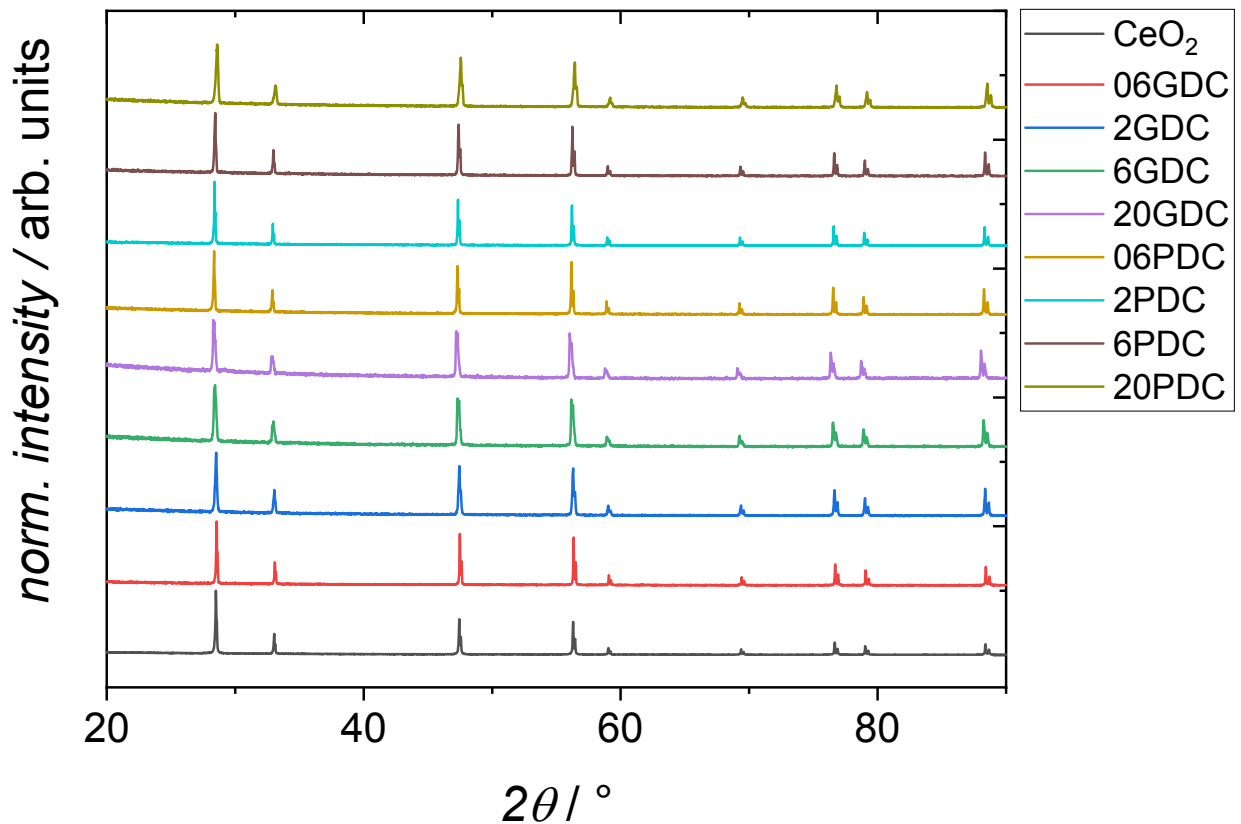
$$\mathfrak{R}_0 = \bar{k}_2 K_1 K(T)^{-1/4} p(O_2) [V_o^{\bullet\bullet}] p(O_2)^{-1/4} [V_o^{\bullet\bullet}]^{-1/2} [O_o^x]^{+1/2} \quad (7)$$

$$\mathfrak{R}_0 \propto p(O_2)^{3/4} \propto [V_o^{\bullet\bullet}]^{1/2}$$

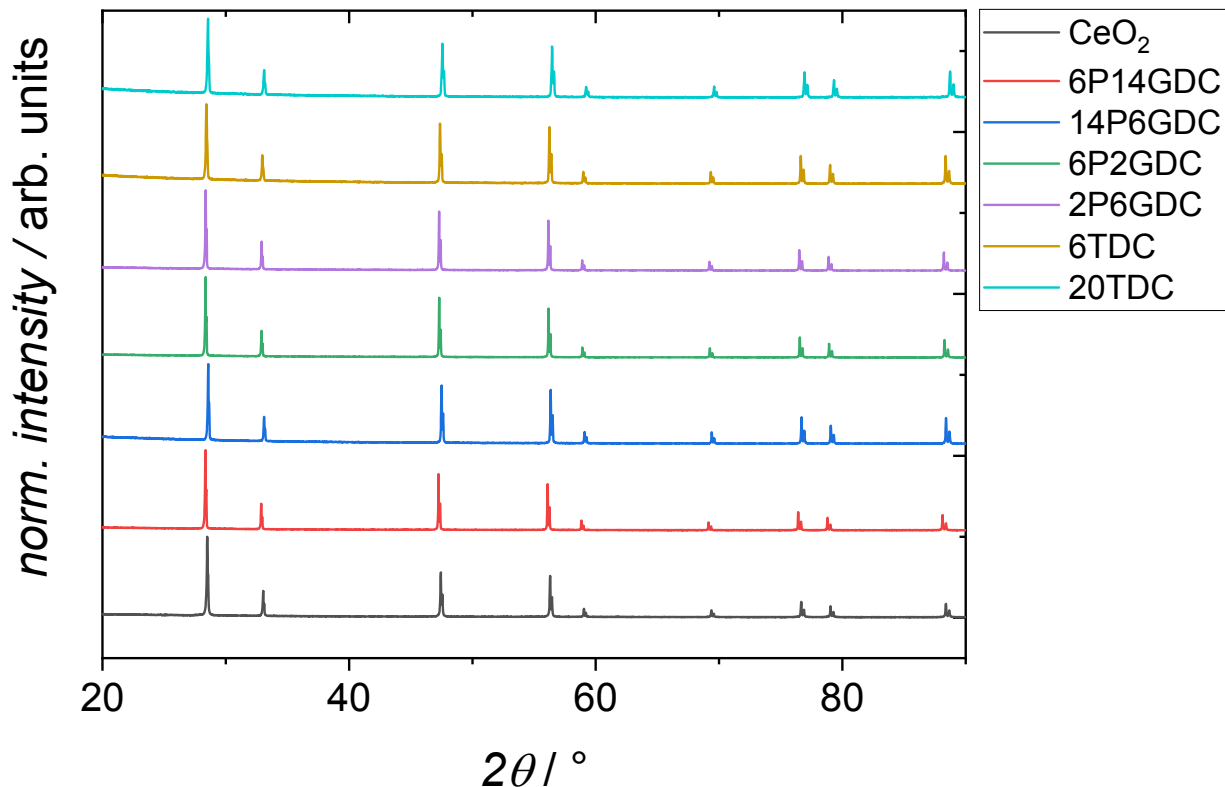
The derivation of the expression for \mathfrak{R}_0 is carried out for forward direction as this is more intuitive, but owing to the principle of microscopic reversibility, the same $p(O_2)$ and $[V_o^{\bullet\bullet}]$ dependencies are obtained when alternatively the backward reaction is considered.

4 XRD Pattern and Lattice Parameters

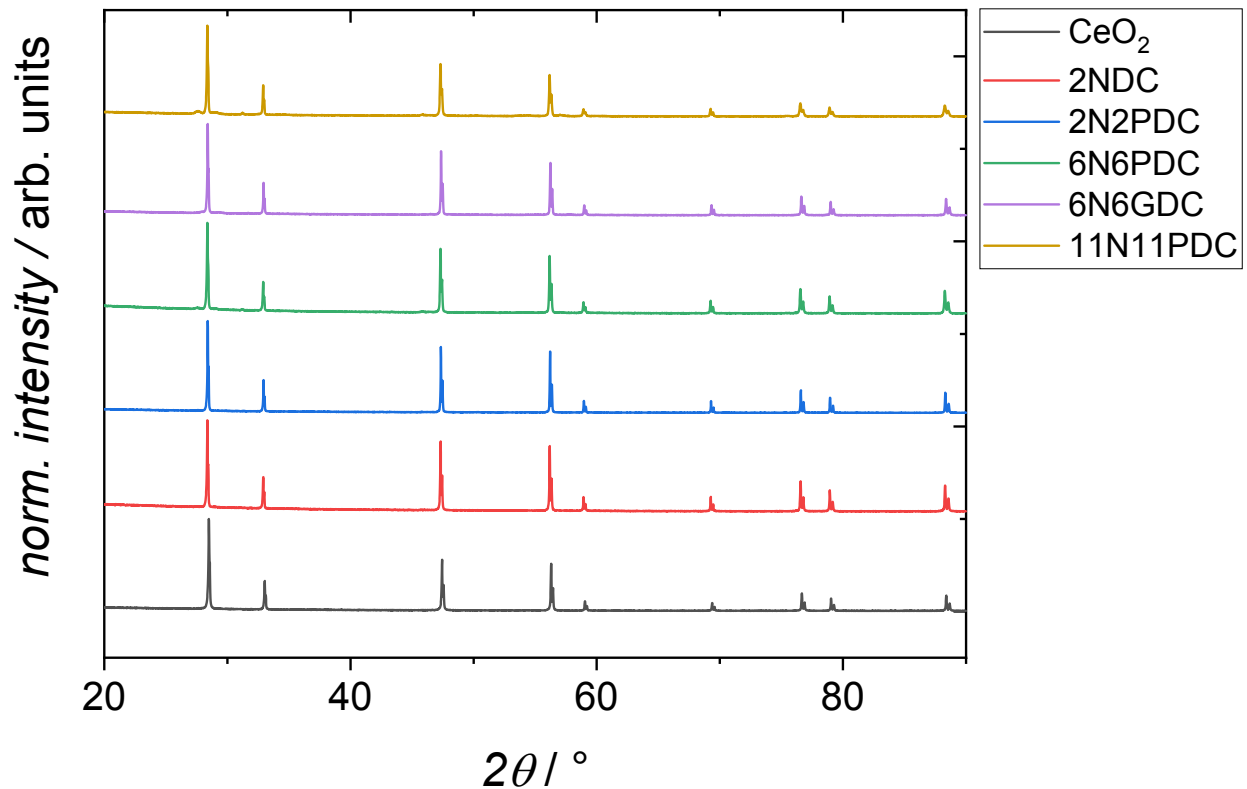
As can be seen from ESI Figure 2 to ESI Figure 4, the doped ceria samples are phase pure. Only 11N11PDC shows a small impurity of a second phase. The lattice parameters are given in ESI Table 2 and Fig. 2b of the main paper.



ESI Figure 2: XRD patterns of undoped ceria, GDC and PDC.



ESI Figure 3: XRD patterns of undoped ceria, Pr/Gd co-doped ceria, and TDC.

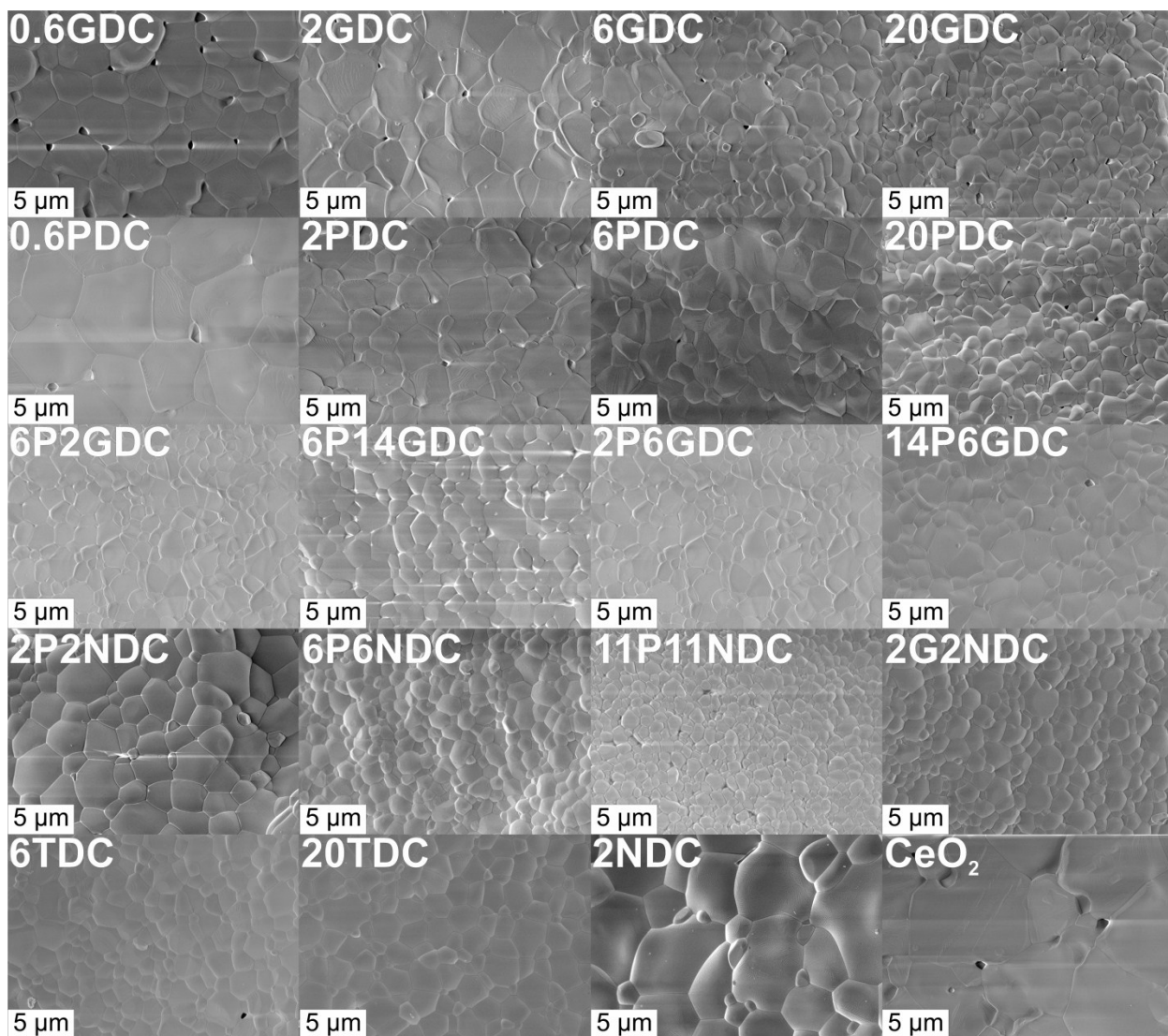


ESI Figure 4: XRD patterns of undoped ceria, 2NDC and equimolar doped Pr/Nb and Gd/Nb co-doped ceria.

ESI Table 2: Lattice Parameter a of Pr, Tb, Gd and Nb co-doped Ceria, obtained from particles which were used in the PIE experiment.

Sample	Lattice Parameter a / Å
CeO ₂	5.4098
06GDC	5.4115
2GDC	5.4113
6GDC	5.4129
20GDC	5.4216
06PDC	5.4075
2PDC	5.4077
6PDC	5.4067
20PDC	5.4056
6TDC	5.4066
20TDC	5.3910
2P6GDC	5.4126
6P2GDC	5.4081
6P14GDC	5.4179
14P6GDC	5.4142
11P11NDC	5.4142
6P6NDC	5.4092
2P2NDC	5.4091
6G6NDC	5.4048
2NDC	5.4080

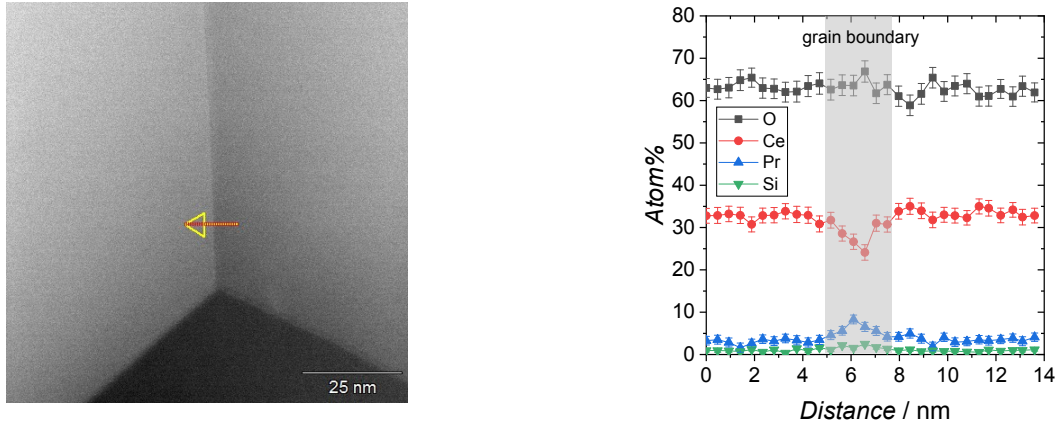
5 SEM images of doped Ceria



ESI Figure 5: SEM images of the surface of doped ceria particles used in the PIE experiments. The grain sizes range from 0.5 to 5 μm and almost no porosity can be found on the surface.

6 EDX Analysis of 6PDC

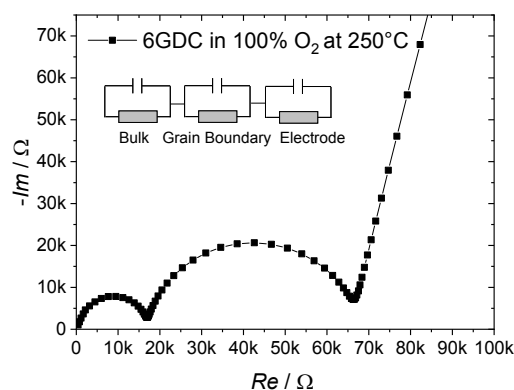
Elemental analysis by TEM was performed on 6PDC particles prior to isotope exchange measurements. In comparison to accumulation of Pr at the surface, the accumulation at the grain boundaries is stronger. No significant content of Si (which is occasionally reported as an impurity in ceria ceramics) was found at the boundaries.



ESI Figure 6: Left: Location and direction of the performed line scan at a grain boundary of 6PDC. Right: at% of Pr, Ce, Si, and O along the line scan.

7 EIS data for GDC and PDC

Electrochemical impedance spectroscopy (EIS) was measured on dense pellets obtained by the same preparation route as mentioned in section 2.1 as a function of temperature and oxygen partial pressure (100, 1, and 0.01 % O₂) by an Alpha-A High Performance Frequency analyzer (Novocontrol Technologies). The samples (bars, approx. 4 x 3 x 2 mm) were polished and placed in the specimen between two Pt-foils, which served as ion blocking electronic contacts. The impedance spectra were fit by an equivalent circuit according to the inset of ESI Figure 7 with ZView (Scribner Associates).



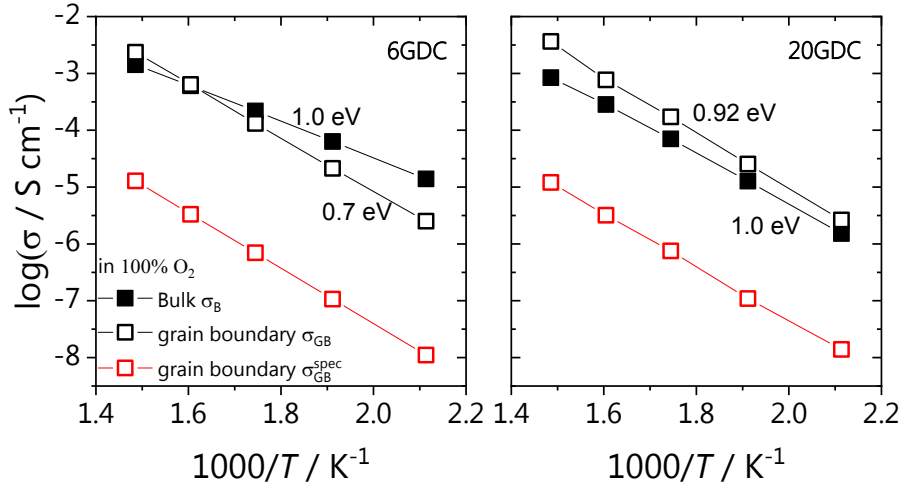
ESI Figure 7: Impedance spectra of 6GDC in 100 % O₂ atmosphere at 250 °C.

In ESI Figure 8 the conductivity measured in 100 % O₂ is depicted as function of temperature. The conductivity of the bulk and the total conductivity of the grain boundary are very close together indicating that the grain boundaries are almost

nonblocking, in particular at the high temperatures of the PIE experiment. The specific grain boundary conductivity (σ_{GB}^{spec}) was calculated according to ref.¹²

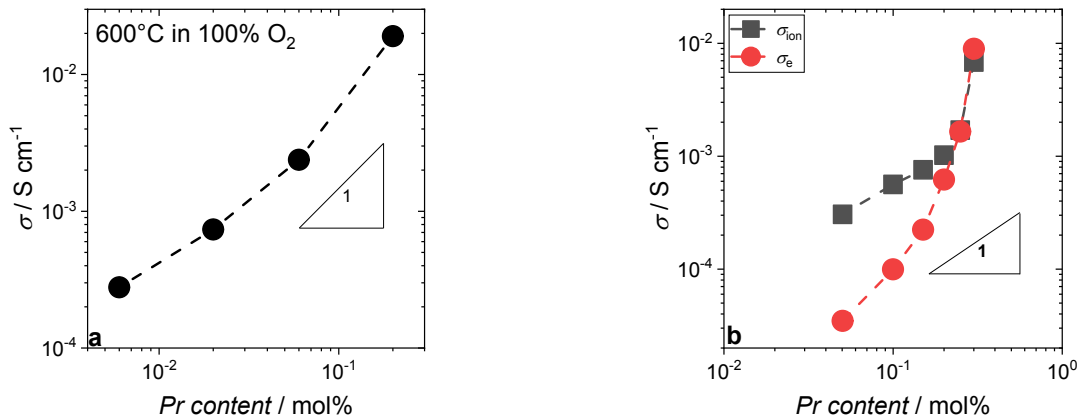
$$\sigma_{GB}^{spec} = \frac{1}{R_{GB}} \frac{L C_B}{A C_{GB}} \quad (8)$$

where R_{GB} is the resistance of the grain boundary semicircle, L , and A are the thickness and area of the sample, C_B , and C_{GB} are the bulk and grain boundary capacitance respectively (brick layer model). Corresponding to the slightly blocking character of the grain boundaries, σ_{GB}^{spec} is always below σ_{bulk} .



ESI Figure 8: Conductivity versus Temperature, obtained by electrochemical impedance spectroscopy in 100 % O₂.

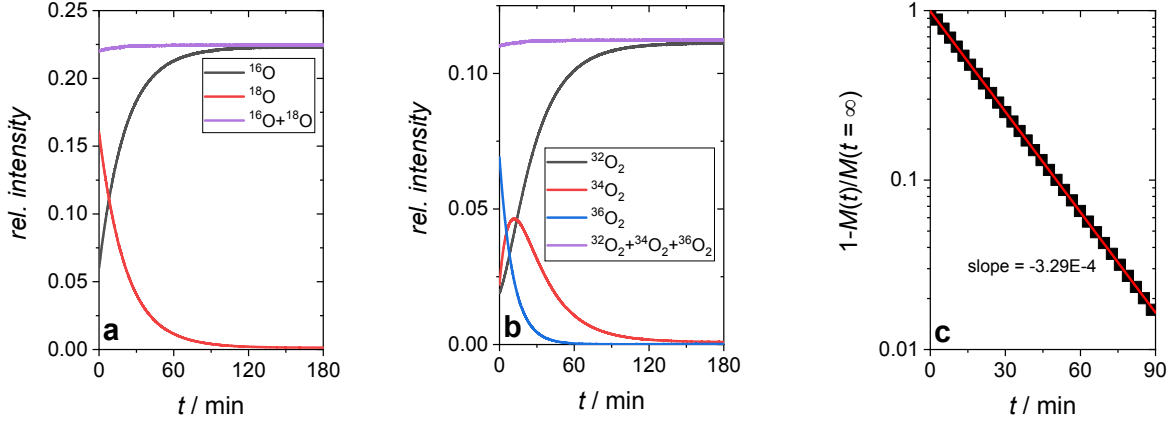
In ESI Figure 9a, the total (ionic + electronic) conductivity of PDC obtained at 600 °C versus Pr dopant content is plotted. With increasing $[Pr]$ the conductivity increases a bit steeper than linear, indicating the broadening of the Pr impurity band. This effect of the broadening impurity band becomes even more obvious when the electronic conductivity is extracted from the total conductivity as done in ref.¹³ and shown in ESI Figure 9b.



ESI Figure 9: Left: Conductivity versus Pr dopant content, obtained by electrochemical impedance spectroscopy in 100 % O₂ and at 600 °C. Right: Shuk *et al.*¹³ ionic and electronic conductivity.

8 Isothermal Isotope Exchange of 20PDC

Isothermal isotope exchange measurement on 100 mg 20PDC particles was performed with the PIE experimental setup in 10 % O₂ atmosphere and a flow rate of 7 mL/min. The sample was equilibrated in ¹⁸O atmosphere for 6 h before abrupt switching to ¹⁶O. The raw data for IIE is depicted in ESI Figure 10a-b and the fit in c.



ESI Figure 10: Raw data for IIE. Left: Fractions of gas phase ¹⁶O and ¹⁸O. Middle: Fractions of gas phase ³²O₂, ³⁴O₂ and ³⁶O₂. Right: Fit of normalized accumulated ¹⁶O.

The exchange rate k^* was calculated according to (see, e.g., ref.^{14, 15})

$$\frac{M(t)}{M(t = \infty)} = 1 - \exp\left(-\frac{3k^* t}{r_p}\right) \quad (9)$$

Where $M(t)$ is the accumulated ¹⁶O in the sample at time t , and $M(t = \infty)$ the total amount of ¹⁶O incorporated into the sample in equilibrium and r_p represents the mean radius of the particles (here $\approx 40 \mu\text{m}$).

9 Exponential Prefactors of GDC and PDC in the Arrhenius Diagram

In ESI Table 3, the exponential prefactors A of GDC and PDC are listed. They

were calculated according to $\log(\eta_0 \text{ mol}^{-1} \text{ s m}^2) = \log(A) - \frac{E_a}{RT}$.

ESI Table 3: Extracted exponential prefactors for GDC and PDC

Sample	A	Sample	A
20GDC	4.0×10^4	20PDC	1.6×10^9
6GDC	5.0×10^6	6PDC	2.5×10^7
2GDC	2.0×10^6	2PDC	5.0×10^5
06GDC	1.1×10^8	06PDC	6.3×10^5

10 References

- 1 D. Poetzsch, R. Merkle and J. Maier, *J. Electrochem. Soc.*, 2015, **162**, F939-F950.
- 2 S. Kim and J. Maier, *J. Electrochem. Soc.*, 2002, **149**, J73-J83.
- 3 M. A. Frechero, M. Rocci, G. Sanchez-Santolino, A. Kumar, J. Salafranca, R. Schmidt, M. R. Diaz-Guillen, O. J. Dura, A. Rivera-Calzada, R. Mishra, S. Jesse, S. T. Pantelides, S. V. Kalinin, M. Varela, S. J. Pennycook, J. Santamaria and C. Leon, *Sci. Rep.*, 2015, **5**, 9.
- 4 C. Balaji Gopal, M. García-Melchor, S. C. Lee, Y. Shi, A. Shavorskiy, M. Monti, Z. Guan, R. Sinclair, H. Bluhm, A. Vojvodic and W. C. Chueh, *Nat. Commun.*, 2017, **8**, 15360.
- 5 W. C. Chueh, A. H. McDaniel, M. E. Grass, Y. Hao, N. Jabeen, Z. Liu, S. M. Haile, K. F. McCarty, H. Bluhm and F. El Gabaly, *Chem. Mater.*, 2012, **24**, 1876-1882.
- 6 C. B. Gopal, F. E. Gabaly, A. H. McDaniel and W. C. Chueh, *Adv. Mater.*, 2016, **28**, 4692-4697.
- 7 Z. A. Feng, F. El Gabaly, X. Ye, Z.-X. Shen and W. C. Chueh, *Nat Commun*, 2014, **5**.
- 8 A. F. Zurhelle, X. R. Tong, A. Klein, D. S. Mebane and R. A. De Souza, *Angew. Chem. Int. Ed.*, 2017, **56**, 14516-14520.
- 9 D. S. D. Gunn, J. A. Purton and S. Metz, *Solid State Ion.*, 2018, **324**, 128-137.
- 10 Q. Lu, G. Vardar, M. Jansen, S. R. Bishop, I. Waluyo, H. L. Tuller and B. Yildiz, *Chem. Mater.*, 2018, **30**, 2600-2606.
- 11 I. Denk, J. Claus and J. Maier, *J. Electrochem. Soc.*, 1997, **144**, 3526-3536.
- 12 J. Fleig and J. Maier, *J. Eur. Ceram. Soc.*, 1999, **19**, 693-696.
- 13 P. Shuk and M. Greenblatt, *Solid State Ion.*, 1999, **116**, 217-223.
- 14 E. N. Armstrong, K. L. Duncan and E. D. Wachsman, *Phys. Chem. Chem. Phys.*, 2013, **15**, 2298-2308.
- 15 Y.-L. Huang, C. Pellegrinelli and E. D. Wachsman, *ACS Catalysis*, 2016, **6**, 6025-6032.